Materials Advances

ROYAL SOCIETY OF CHEMISTRY

COMMUNICATION

View Article Online
View Journal | View Issue

Check for updates

Cite this: *Mater. Adv.*, 2025, 6, 6243

Received 23rd April 2025,
Accepted 25th July 2025

DOI: 10.1039/d5ma00390c

rsc.li/materials-advances

# Additive manufacturing of commercially pure magnesium and Mg–2Ag–2Sn alloys by *in situ* alloying during laser powder bed fusion

Ajit Kumar,[ab] Muralidhar Yadav,[ac] C. P. Paul,[d] Sanjay Mishra,[d] Satyam Suwas[a] and Kaushik Chatterjee *[a]

**Despite the advancements in additive manufacturing to prepare personalized implants of complex geometries, the additive manufacturing of Mg alloys has posed significant challenges. In this work, commercially pure (Cp) Mg and Mg–2Ag–2Sn alloys were additively manufactured *via* laser-powder bed fusion (L-PBF). Elemental powders were ball-milled to prepare the alloy powder for L-PBF. Optimized fabrication parameters were determined by preparing tracks at varying laser parameters. Non-spherical powders could be successfully utilized in this process. Microstructural analysis by optical microscopy, X-ray diffraction, scanning electron microscopy, and energy-dispersive X-ray spectroscopy revealed the presence of different phases, including some Al uptakes from the substrate. Hardness studies revealed a 63% increase in the hardness of the Mg–2Ag–2Sn alloy compared to Cp Mg. Additionally, the fabricated Mg–2Ag–2Sn alloy system demonstrated almost two-and-a-half-fold improved corrosion resistance than Cp–Mg, making it potentially viable for orthopaedic implants. This study demonstrates the fabrication of Cp Mg *via* additive manufacturing by laser powder bed fusion (LPBF), accompanied by systematic optimization of the processing parameters. Furthermore, a comparative analysis between pure Mg and the Mg–2Ag–2Sn alloy is conducted to evaluate their properties. The results demonstrate that LPBF is a promising process for the advanced manufacturing of Mg-based alloys for biomedical applications.**

## 1. Introduction

Magnesium (Mg) alloys are some of the most promising materials for biodegradable implants and lightweight structures and are often regarded as the metals of the future.[1–5] However, biomedical applications of Mg alloys are limited by their rapid degradation in aqueous media.[6–9] Toward modulating the corrosion rate, researchers are increasingly focused on developing novel Mg-alloys that combine good mechanical properties, degradation rates, and bioactivity for next-generation resorbable implants.[7,9–12] Specifically, silver (Ag) and tin (Sn) have attracted much attention as alloying elements for enhancing the biomedical performance of pure Mg for orthopedic applications.[13,14]

In additive manufacturing, laser powder bed fusion (LPBF) offers several advantages for producing lightweight and customized products.[3,8,15] Fabrication of Mg alloys by LPBF is of much interest to prepare parts for biomedical applications and other industries.[3,10] Owing to its low melting temperature and high propensity for oxidation, additive manufacturing of Mg poses many technical challenges. Additive manufacturing of a few Mg alloys *via* LPBF has been attempted with limited success.[2,3,7–10,15,16] Some reports on the processing of commercially pure (Cp) Mg LPBF alloys are available in the literature. However, all these studies used pre-alloyed spherical powders, and the processing routes to obtain these powders make them expensive. A key bottleneck in processing novel alloys by LPBF is the lack of pre-alloyed powders. *In situ* alloying, employing mixed powder feedstocks in LPBF, offers an alternate, flexible route to explore a vast compositional space and elemental combinations, enabling the creation of functionally graded materials.[17,18] In recent years, we and others have explored *in situ* alloying of elemental powders to prepare alloys by LPBF.[19–21]

Conventionally, most studies on additive manufacturing of alloys by LPBF utilize pre-alloyed powders prepared by atomization from a homogenous alloy melt. This approach yields excellent starting compositional homogeneity upon melting during LPBF.[22] Pre-alloyed powders also tend to exhibit consistent flow behavior and well-characterized solidification windows, reducing local chemistry variations or unexpected eutectic formation. However, pre-alloyed powders are more expensive because melting, homogenizing, and gas atomizing

---

[a] *Department of Materials Engineering, Indian Institute of Science, C.V. Raman Avenue, Bangalore 560012, India. E-mail: kchatterjee@iisc.ac.in*
[b] *Department of Smart Manufacturing, New Age Makers Institute of Technology (NAMTECH), Gandhinagar, Gujarat 382355, India*
[c] *School of Materials Science and Engineering, Nanyang Technological University, 50 Nanyang Avenue, 639798, Singapore*
[d] *Laser Materials Processing Laboratory, RRCAT, Indore, 452013, India*

a fully alloyed material adds processing steps and higher energy costs. In contrast, *in situ* alloying and mixing elemental powders to form alloys directly in the build chamber can markedly lower raw-material costs by using simpler, often cheaper elemental feeds. Liang *et al.* showed that adding 1 wt% Y to ZK60 *via* ball milling reduces powder costs compared to sourcing dedicated gas-atomized ZK60-Y feedstock. However, the use of mixed elemental powders can generate local compositional inhomogeneities owing to incomplete mixing or localized segregation, which can degrade mechanical properties.

Additionally, elemental-powder routes also bring distinct process challenges. Individual powders have different melting points, densities, and surface oxides, so their fluidity under the melt pool can vary significantly. During *in situ* alloying, disparate oxides can agglomerate or form large oxide inclusions in the melt pool, disrupting the flow and promoting porosity. By contrast, pre-alloyed powders already include stable oxides that minimally disrupt fluidity. Despite these challenges, *in situ* alloying presents a compelling approach for developing novel alloys with tailored properties.

In the present work, Cp–Mg and Mg–2Ag–2Sn alloys were processed by LPBF to establish the feasibility of this processing route. Pre-mixed elemental powders were used as feed for LPBF toward preparing the alloy. The effects of process parameters on the microstructure, hardness, and corrosion were investigated. Moreover, a comparative study between the microstructure and biocorrosion was performed for Cp–Mg and Mg–2Ag–2Sn prepared *via* LPBF. The approach proposed in this study can be used as a viable method for preparing additively manufactured parts of magnesium alloys, with implications for creating personalized resorbable implants.

## 2. Materials and methods

To prepare alloy powder, Cp–Mg particles, tin (Sn) particles (with an average particle size (APS) of 45 μm), and silver (Ag) particles (with an APS of 6 μm) were blended in a planetary ball mill (Fig. S1 and S2). The detailed powder processing procedure can be found in the SI (Section SA). The blended powders were sieved and dried in an oven at 120 °C. In the customized setup of LPBF, 200 g of dried powder was poured into the chamber cavity, and 75 μm of powder was spread over the aluminum substrate (∅ 50 mm × 10 mm) using a spreader after raising the chamber by the same height. This process was continued until a track thickness of 1 mm was reached. A fiber laser (IPG Photonics (India) Pvt. Ltd) with a maximum power of 500 W (air-cooled) and a wavelength of 1070 nm was used for the experiments. Printing was performed in a vacuum chamber maintained at $10^{-5}$ bar and oxygen <5 ppm with continuous argon gas purging. Table 1 compiles different combinations of laser power (W) and scanning speed (m $s^{-1}$) for LPBF to print alloy tracks using a fixed hatch spacing of 1 mm and a thickness of 75 μm. The energy density (J $mm^{-3}$) was calculated using the formula given below.

$$\text{Energy density} = \frac{P}{S \cdot V \cdot t} \tag{1}$$

where $P$ = laser power; $S$ = hatch spacing; $V$ = scan speed; and $t$ = layer thickness.

Table 1 LPBF process parameters for Mg–2Ag–2Sn

| Track number | Laser power (W) | Scan speed (m $s^{-1}$) | Energy density (J $mm^{-3}$) |
|---|---|---|---|
| T1 | 200 | 0.02 | 133 |
| T2 | 200 | 0.03 | 88 |
| T3 | 200 | 0.04 | 66 |
| T4 | 240 | 0.02 | 160 |
| T5 | 240 | 0.03 | 107 |
| T6 | 240 | 0.04 | 80 |
| **T7** | **280** | **0.02** | **188** |
| T8 | 280 | 0.03 | 124 |
| T9 | 280 | 0.04 | 93 |
| T10 | 320 | 0.02 | 213 |
| **T11** | **320** | **0.03** | **142** |
| T12 | 320 | 0.04 | 107 |
| T13 | 360 | 0.02 | 240 |
| **T14** | **360** | **0.03** | **160** |
| T15 | 360 | 0.04 | 120 |
| T16 | 400 | 0.02 | 267 |
| **T17** | **400** | **0.03** | **178** |
| T18 | 400 | 0.04 | 133 |
| T19 | 440 | 0.02 | 293 |
| **T20** | **440** | **0.03** | **196** |
| T21 | 440 | 0.04 | 150 |
| T22 | 300 | 0.02 | 200 |
| T23 | 300 | 0.03 | 133 |
| T24 | 300 | 0.04 | 100 |

Porosity and crack density were quantified by thresholding SEM images of polished cross-sections in ImageJ to create binary masks of defects. The pore area was measured as the sum of connected void-pixel areas. Porosity (%) was calculated as $(\Sigma A_{\text{pores}}/A_{\text{total}}) \times 100$. Cracks were identified as elongated features (aspect ratio >5) in the same mask, with the crack density given by $N_{\text{cracks}}/A_{\text{total}}$ (cracks $mm^{-2}$). Each value represents the mean ± SD over five non-overlapping 0.35 $mm^2$ fields per track.

An X-ray diffractometer (Bruker, D8 ADVANCE, operated at 40 kV and 30 mA) equipped with Cu-Ka radiation ($\lambda$ = 1.54 Å) was used to analyze the phases. X-ray diffraction (XRD) patterns were recorded in the $2\theta$ range of 30–80° with a step size of 0.02° and a scan rate of 2° $min^{-1}$. Microstructural analysis was carried out using a TESCAN scanning electron microscope (SEM, MIRA3) equipped with an energy-dispersive spectrometer (EDS). Prior to analysis, the samples were mechanically ground, polished, and etched using an acetic-picrate solution. Using ImageJ software (version 1.42), a quantitative image analysis was carried out to extract quantitative information, such as the grain size and porosity, from microstructure images.

The corrosion assessment of the alloy was conducted in simulated body fluid (SBF), and the details can be found in the SI (Section SB).[23–25] Tafel analysis of the corrosion plots was carried out using the ECLab software (Version 10.38) BioLogic (2014).[26]

For Vickers microhardness measurements, samples were polished up to 5000 emery paper, followed by diamond polishing. A 0.5 kgf load was applied to the mirror-polished sample surface for 15 seconds. Five indentations were taken at different positions of the sample.

The alloy powder prepared by ball milling was dried at 120 °C to attain the flowability of powders and then processed *via* LPBF to prepare the tracks and circular parts of the Mg–2Ag–2Sn alloy. In the current study, elemental powders were mechanically milled and sieved up to 25 μm, which was found to be well-suited for LPBF, and printed successfully (Fig. S1 and S2).

## 3. Results and discussion

Different laser energy densities were used to print Cp–Mg and Mg–2Ag–2Sn tracks to evaluate the feasibility of additive manufacturing by LPBF. A short stripe width scanning strategy, combined with high-power, high-speed scanning, can produce large, stable melt pools with low aspect ratios.[27] The short stripe width strategy involves using short scanning vectors (on the scale of 1 mm), minimizing the cooling time between adjacent scans. This results in a brief "thermal rest time," facilitating the transition from a typical single-track to larger melt pools. This approach has been shown to reduce porosity, improve homogeneity, and increase printing speed compared to conventional Gaussian laser scanning. The printing strategy used in the current study to print the alloy using the elemental powders using LPBF follows a similar type of strategy to obtain highly dense fabricated parts.

Fig. S3 and S4 present the LPBF chamber, illustrating the powder bed along with the printed tracks and circular parts. Fig. 1(a)–(e) depicts the SEM micrographs of the tracks for various conditions (T11, T14, T17, T7, and T20; refer to Table 1), showing noticeable track thicknesses of 40–70 μm. Other conditions did not yield continuous and uniform tracks. Porosity and crack density analyses were performed for these tracks using ImageJ software for these five conditions that yielded continuous tracks, as listed in Table 1. Among these conditions, T17 showed the highest thickness of 70 μm.

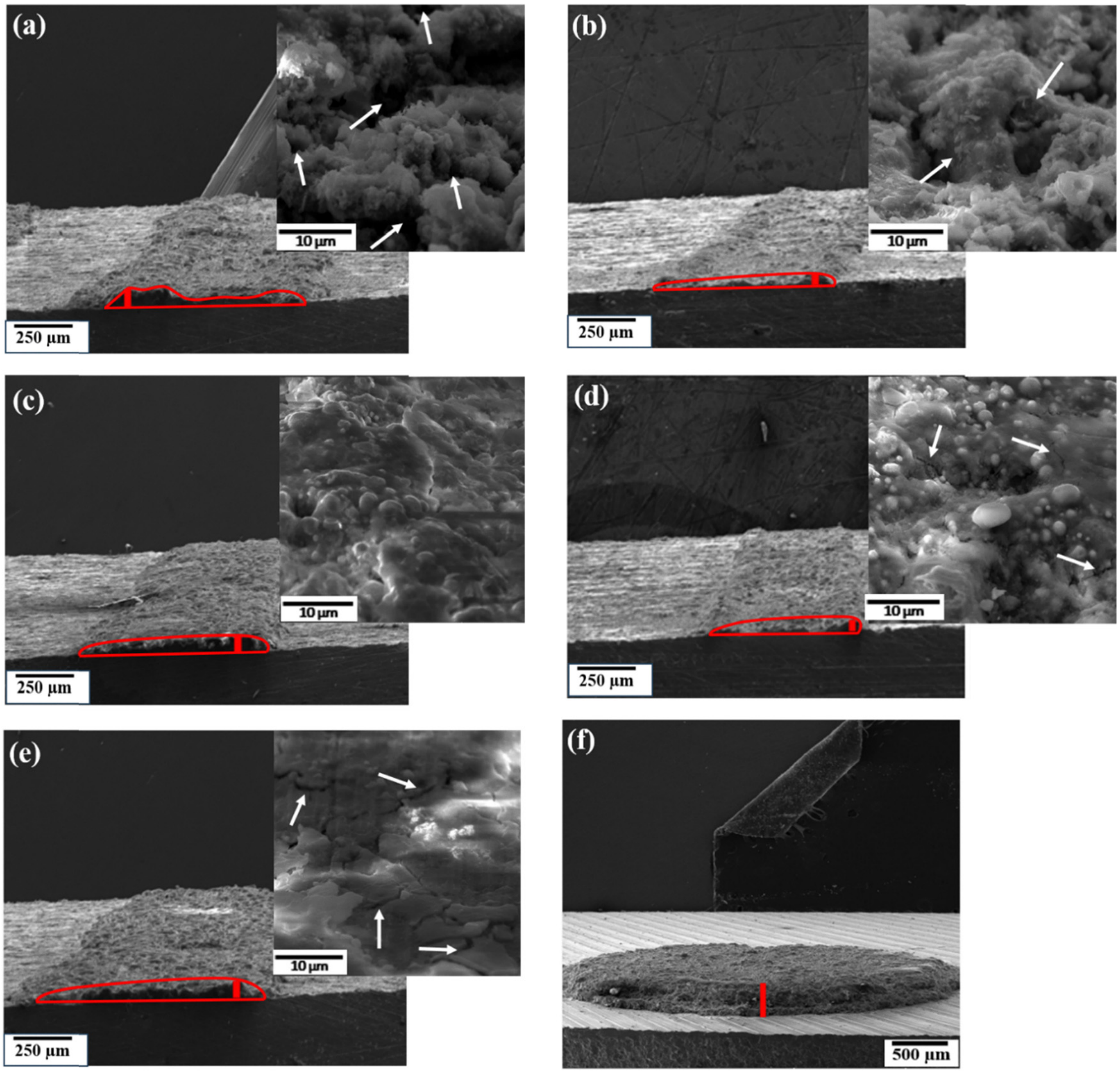

Fig. 1 SEM images of tracks prepared at different parameters (a) T11, (b) T14, (c) T17, (d) T7, and (e) T20 and (f) circular parts printed at optimized parameters (T17).

At a relatively low energy density of 142 J mm$^{-3}$, larger pores were observed in T11 (white arrows in Fig. 1(a)). For T14, at an energy density of 160 J mm$^{-3}$, enhanced fusion and necking between particles were observed (marked by white arrows), which led to a significant reduction in the pores (Fig. 1(b)). Furthermore, as the energy density increased to 178 J mm$^{-3}$ for T17, a complete fusion of the particles was found and resulted in dense and uniform printing with minimal pores (red color in Fig. 1(c)). However, even at a higher energy density of 188 J mm$^{-3}$ for T7, initiation of cracks was observed between the adjacent layers (Fig. 1(d)), which further intensified to 196 J mm$^{-3}$ for T20 (white arrows in Fig. 1(e)).

A relatively low laser energy density (Fig. 1(a)) caused the powder layer to melt only partially, resulting in pockets of non-dense powder. Conversely, cracks at excessively high energy densities (Fig. 1(e)) likely arose due to residual stresses owing to the thermal contraction caused by excessive melting and rapid solidification of the tracks. Thus, laser energy densities beyond 196 J mm$^{-3}$ caused the tracks to accumulate considerable thermal stresses, resulting in significant defects. Taken together, T17 yielded tracks with a complete fusion of particles with minimal defects.

In the scientific literature, Ling *et al.* reported an energy density of 53.6–95.2 J mm$^{-3}$ for printing dense WE43 parts using LPBF, whereas Jauer *et al.* and Gangireddy *et al.* reported 40.7 J mm$^{-3}$ and 238.1 J mm$^{-3}$, respectively, for the same.[16,22,28] ZK60 parts were successfully printed by Liang *et al.* with 292 J mm$^{-3}$ energy density, whereas Wei *et al.* utilized 416.66 J mm$^{-3}$.[29] In a different study, 166.7 J mm$^{-3}$ was determined to be optimal to print AZ91 and AZ31 alloys.[30] Thus, these values can range widely from 50–420 J mm$^{-3}$ based on the alloy printed. Notably, all the earlier studies were performed with pre-alloyed powders.

This study is distinct from the conventional approach of using spherical pre-alloyed powders in laser powder bed fusion (LPBF) and instead utilizes non-spherical, ball-milled elemental powders (Mg, Ag, Sn). Unlike costly pre-alloyed WE43 and ZK60 powders—produced *via* melt homogenization and gas atomization—the elemental approach enables flexible, on-demand composition control (*e.g.*, Mg–2Ag–2Sn) without the need for an intermediate alloying step. Despite its lower cost, the elemental route achieves comparable results, such as fine α-Mg grain sizes (<10 μm), high density (∼99%), and enhanced mechanical and corrosion properties. However, while pre-alloyed powders offer consistent composition and fluidity, *in situ* alloying demands strict control over powder mixing, oxygen content, and melt-pool behavior to avoid defects like segregation or cracking.

The interaction of the laser with the powder, particularly molten pool evolution, directly affects the final part quality. At low energy density values, incomplete melting leads to insufficient liquid formation, resulting in high-viscosity molten pools that cannot spread, causing lack-of-fusion pores. Higher energy density ensures complete melting and induces keyhole formation due to metal vapor recoil, enhancing heat and mass transfer *via* Marangoni convection, which further leads to a reduction in porosity and other defects within the printed material.[31] An increase in the energy density reduces defect density to yield dense parts, such that the T17 condition offers the best parameters among the different conditions studied here. Excessive energy density increases evaporation, aggravating the keyhole effect and trapping vapor during solidification, leading to keyhole defects. Mg alloys, with their lower boiling points and higher vapour pressures, are more prone to evaporation, preventing stable keyhole formation.[16] In the current study, 178 J mm$^{-3}$ provided sufficient energy density to fuse particles and form melt pools desirable to yield highly dense parts. The process parameters of T17 were subsequently used to prepare circular samples of the Mg–2Ag–2Sn alloy (Fig. 1(f)). The EDS analysis results of the track and circular part are shown in Fig. S5. Notably, the edges of all samples appeared thicker, which arises as the laser reaches the ends of the track to print a layer. It stops momentarily before restarting to print a new layer, thereby causing extended melting and solidification. As the edges are directly exposed to the atmosphere, they quickly dissipate heat and solidify rapidly as they cool. However, in the case of T11, proper melting and diffusion could not be achieved due to insufficient energy density. In contrast, since the laser stops for a considerable amount of time at the ends, this allows for melting and solidification, further leading to higher material printing and thicker edges than those found in the center (red color in Fig. 1(a)).

The XRD peaks of the additively manufactured Cp–Mg and Mg–2Ag–2Sn alloy revealed the presence of α-Mg, $Mg_{0.42}Al_{0.58}$, $MgAl_2O_4$, and AlMg peaks in both the samples (Fig. 2). The high laser energy employed during the LPBF process appears to have induced the formation of various Mg–Al phases in the fabricated samples, likely as a result of interaction with the aluminum substrate. These observations corroborate the EDS findings (Fig. 3(c) and Fig. S5(c), (d)). The presence of $Mg_{0.42}Al_{0.58}$, $MgAl_2O_4$, and AlMg phases could be eliminated by replacing the Al substrate with Mg. The Mg–2Ag–2Sn alloy

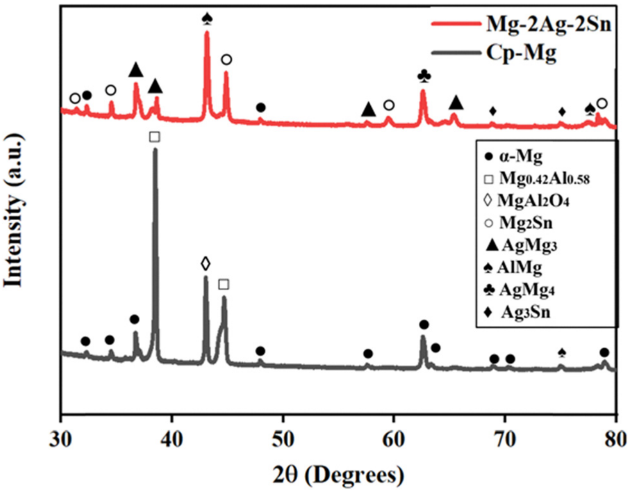

Fig. 2 XRD patterns of Cp–Mg and Mg–2Ag–2Sn circular samples prepared at optimized process parameters (T17).

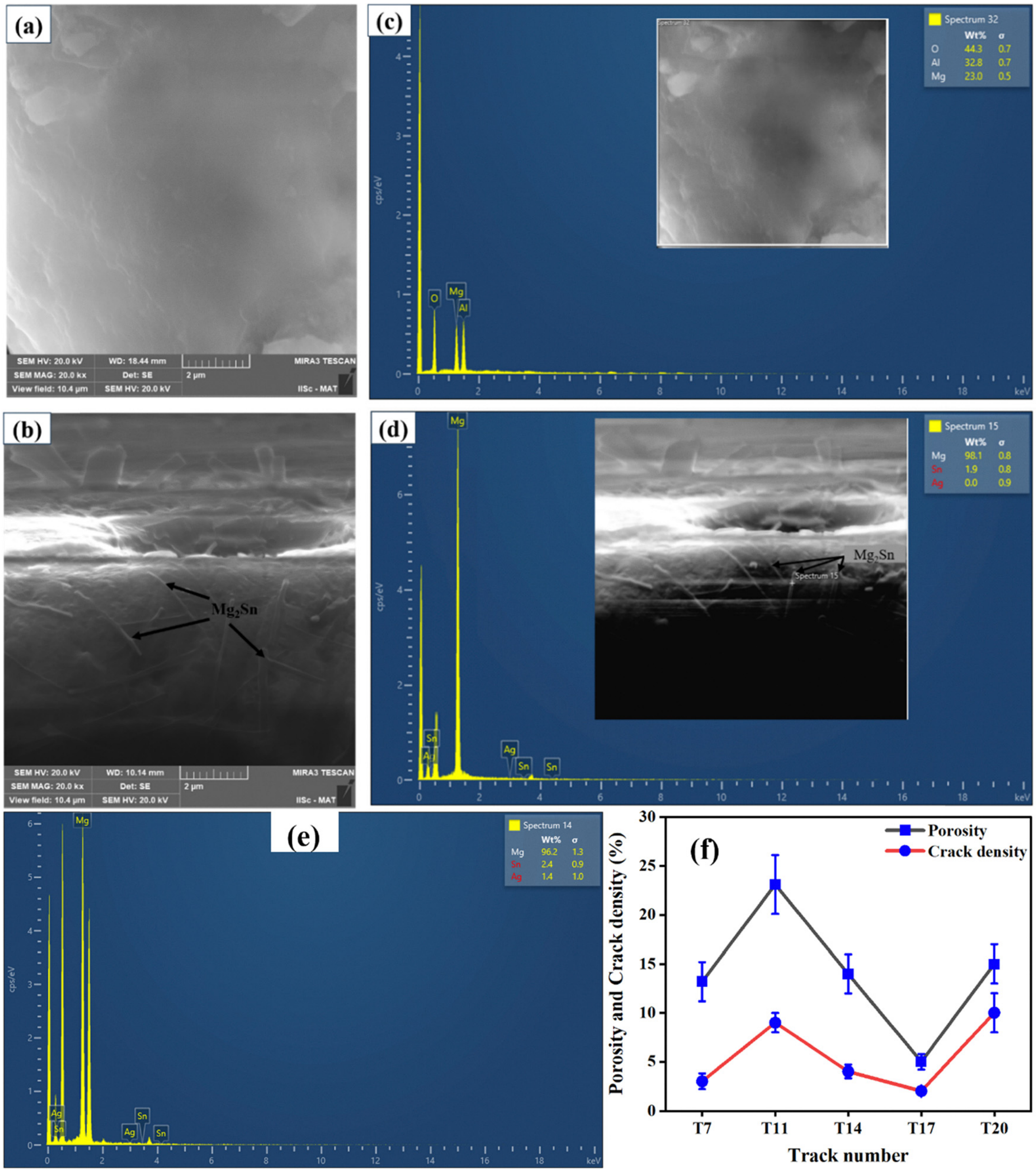

Fig. 3 (a) and (b) SEM micrographs of Cp–Mg and Mg–2Ag–2Sn alloys, respectively, and (c)–(e) their corresponding EDS spectra of alloy (f) porosity and crack density *vs.* track number plot for different tracks.

revealed additional characteristic peaks of intermetallic phases of $Mg_2Sn$, $AgMg_3$, $AgMg_4$, and $Ag_3Sn$. These intermetallic phases are attributed to rapid non-equilibrium cooling, forming different metastable phases.[3,9]

In Fig. 3b, nail-like features are visible in the Mg–2Ag–2Sn alloy processed by optimized laser parameters, indicating the presence of $Mg_2Sn$. These observations correlate well with the EDS results shown in Fig. 3(d) and the XRD results (Fig. 2), whereas no such features were observed for the Cp–Mg sample (Fig. 3(a) and (c)), like those reported earlier.[32] In addition, cracks and pores were observed in such alloy systems.[2] SEM and EDS analyses (Fig. 3(b)) reveal that the Mg–2Ag–2Sn alloy contains the $Mg_2Sn$ phase within the predominant Mg-matrix, which manifests as elongated, nail-like precipitates (mean length ≈ 1.2 μm, width ≈ 0.2 μm) within the matrix. X-ray diffraction further identifies additional phases ($AgMg_3$, $AgMg_4$, and $Ag_3Sn$) dispersed throughout the Mg matrix. Moreover, the diffraction data suggest the presence of $Ag_3Sn$ in addition to other phases in the alloy system. Additionally, it can be further inferred that $Mg_2Sn$ with a volume fraction of 4.5% is finely dispersed within the matrix with a significant volume fraction of $Ag_3Sn$ and other phases. Fig. 3(e) indicates the presence of Ag and Sn within the matrix in addition to Mg when the spectrum is taken from the matrix, suggesting the possibility of the formation of different phases, including Ag and Sn. The formation of such phases, especially $Mg_2S$ and $Ag_3Sn$, confirms the formation of a passive layer over the surface of the alloy, thereby protecting it from corrosion.[32] As shown in Fig. 3(f), porosity was quantified from SEM cross-sections of tracks T11–T20, revealing a decrease from ∼23.1% at 142 J $mm^{-3}$ (T11) to a minimum of 5% at 178 J $mm^{-3}$ (T17), followed by an increase to ∼15% at >188 J $mm^{-3}$ due to crack-induced defects. Below ∼150 J $mm^{-3}$, insufficient melting leads to lack-of-fusion porosity, while above ∼190 J $mm^{-3}$, keyholing and Mg vaporization cause cracks and deep voids.[33] The optimal energy density of 178 J $mm^{-3}$ ensures balanced melt-pool dynamics *via* balanced Marangoni convection which promotes melt-pool homogeneity and expels entrapped gas with vapor recoil, resulting in stable, single-track pools with minimized porosity and cracking, as summarized in Table 1,[34] whereas below ∼160 J $mm^{-3}$, porosity falls rapidly as melting improves, and above ∼185 J $mm^{-3}$, defects rise sharply due to keyhole instability and stress cracking.

The composition homogenization of printed tracks in LPBF is governed by the solidification process. Initially, "solute capture" reduces composition differences between supersaturated α-Mg and different phases present in the alloy. Convection in the molten pool further promotes liquid homogenization. He *et al.*'s fluid flow model suggests that convection is driven by buoyancy and Marangoni forces. The dominance of each force can be assessed by the ratio of the surface-tension Reynolds number (Ma) to the buoyancy-related Grashof number (Gr).[35]

$$R_{\mathrm{s/b}} = \frac{\mathrm{Ma}}{\mathrm{Gr}} = \frac{L_{\mathrm{R}} \times \left|\dfrac{\partial y}{\partial T}\right|}{g\rho\delta {L_{\mathrm{b}}}^{3}} \tag{2}$$

Wwhere $L_R$ is the pool radius, half the width of the scanning track, and $\partial\gamma/\partial T$ is the temperature coefficient of surface tension. Other parameters include gravitational acceleration ($g$), material density ($\rho$), thermal expansion coefficient ($\delta$), and the buoyancy force characteristic length ($L_b$), roughly one-eighth of the scanning track width. For a sample fabricated at 178 J/ $mm^{-3}$ with an average track width of 75 μm, $R_{s/b}$ is approximately 15.5 × $10^7$. This suggests that fluid flow is primarily driven by Marangoni convection. The maximum liquid velocity correlates positively with the temperature gradient, which, due to the Gaussian laser distribution and small pool size in LPBF, generates a strong temperature gradient. This enhances Marangoni convection, promoting homogeneous dispersion of Mg and Sn elements.

As shown in Fig. 4a- and b, the microhardness at the cross-section of the aluminum substrate was found to be 32 ± 0.7 HV (mean ± S.D. for $n$ = 5 indents), which matches well with studies reported previously.[36] However, the hardness value at the interface of the aluminum substrate and printed Mg–2Ag–2Sn alloys in Fig. 4c was found to be 54 ± 6 HV ($n$ = 5), which was 70% higher than the hardness of the aluminum substrate. Fig. 4d shows the hardness of the additively manufactured Mg–2Ag–2Sn alloy, which was found to be 133 ± 14 HV ($n$ = 10). The increase in the hardness is due to the presence of the intermetallic phases formed with Sn and Ag, as confirmed by XRD and BSE analyses. The hardness of Cp–Mg printed by LPBF was determined to be 83 ± 7 HV ($n$ = 5), which can be seen in Fig. 4e. The markedly enhanced hardness of the Mg–2Ag–2Sn alloy compared to Cp–Mg is a result of incorporating Sn and Ag into the Mg-based alloy. Sn forms intermetallics, such as $Mg_2Sn$, as confirmed by XRD, which impart hardness to the alloy. Ag also improves hardness *via* grain refinement and solid solution strengthening, and by increasing the number density, size, and volume fraction of $Mg_2Sn$ precipitates.[37–43] By encouraging dispersive precipitation and raising the volume fraction of $Mg_2Sn$ precipitates,[40] Ag can enhance the hardness of Mg–Ag–Sn. Sn refines the precipitates, increases the volume of the secondary phase, and modifies the type of intermetallic phase, thereby increasing their number density. It is reported that this effect enhances age-hardening response at an earlier stage, leading to higher strength and moderate elongation.[44–46] The high hardness of the additively manufactured samples of both alloys results from the combination of dense parts with minimal porosities and homogeneous distribution of the elements. Owing to optimized fabrication parameters, the hardness of both Cp–Mg and Mg–2Ag–2Sn alloys was increased post-printing compared with that of wrought Mg due to the formation of dense parts with reduced porosities.[47] An optimal parameter of printing caused the homogeneous distribution of the elements within the printed alloy, resulting in an alloy with reduced porosity and increased hardness. Thus, T17 was determined to be the optimal condition for printing dense parts.

To qualify as a biomedical material, Mg-alloys must exhibit a good combination of mechanical properties and corrosion resistance. The properties evaluated for the test samples prepared herein were extrapolated using widely applied formulae. The hardness ($H_v$) can be converted to GPa and MPa by multiplying 9.807 and 0.009807, respectively, with the $H_v$ values.[48,49] Furthermore, the elastic modulus ($E$ in GPa) and yield strength ($Y_s$ in MPa) can be obtained using the standard formula[50,51] provided in eqn (3) and (4), and their corresponding values are tabulated in Table 2.

$$E = \frac{H_{\mathrm{v}}}{0.036} \tag{3}$$

$$\mathrm{YS} = \frac{H_{\mathrm{v}}}{3} \tag{4}$$

To validate the calculated yield strength, a comprehensive analysis of the strengthening mechanisms was conducted to quantify the individual contributions of each strengthening factor to the overall yield strength of the LPBF Mg–2Ag–2Sn alloy ($\sigma_{\mathrm{alloy}}$). This was achieved by decomposing the total yield strength into three well-established components, each added to the frictional strength of pure LPBF Mg ($\sigma_0 \approx 214.4$ MPa), as reported in previous studies. The resulting strengthening behavior of the alloy is described by eqn (5).

$$\sigma_{\mathrm{alloy}} = \sigma_{\mathrm{o}} + \Delta\sigma_{\mathrm{SS}} + \Delta\sigma_{\mathrm{Or}} + \Delta\sigma_{\mathrm{HP}} \tag{5}$$

where $\Delta\sigma_{\mathrm{ss}}$ is the solid-solution term, $\Delta\sigma_{\mathrm{Or}}$ comes from the Orowan dispersion, and $\Delta\sigma_{\mathrm{HP}}$ arises from grain refinement (the Hall–Petch effect).[52] Solute atoms create elastic-strain fields that pin dislocations, fine $Mg_2Sn/Ag_3Sn$ particles force

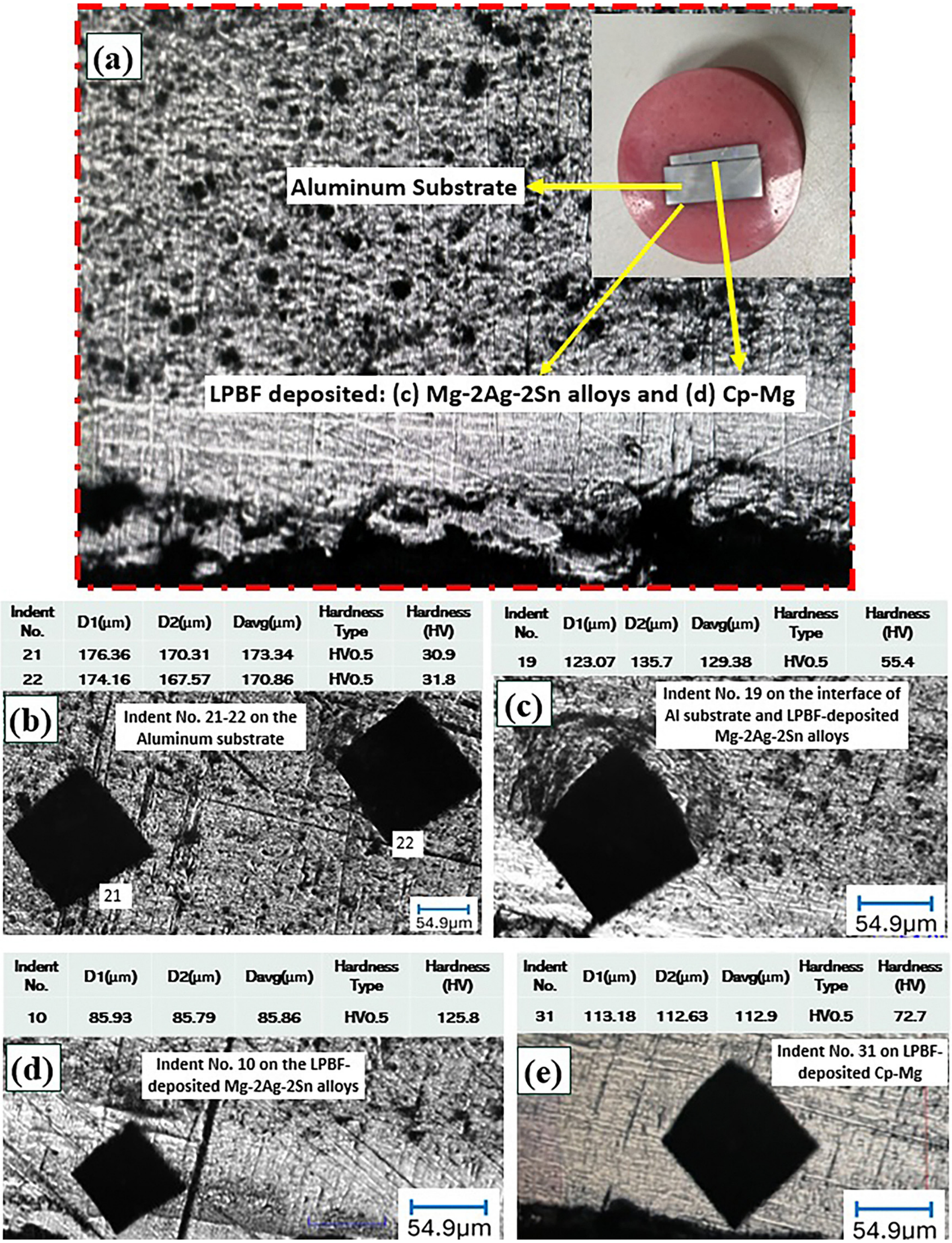

| Indent No. | D1(µm) | D2(µm) | Davg(µm) | Hardness Type | Hardness (HV) |
|---|---|---|---|---|---|
| 21 | 176.36 | 170.31 | 173.34 | HV0.5 | 30.9 |
| 22 | 174.16 | 167.57 | 170.86 | HV0.5 | 31.8 |

| Indent No. | D1(µm) | D2(µm) | Davg(µm) | Hardness Type | Hardness (HV) |
|---|---|---|---|---|---|
| 19 | 123.07 | 135.7 | 129.38 | HV0.5 | 55.4 |

| Indent No. | D1(µm) | D2(µm) | Davg(µm) | Hardness Type | Hardness (HV) |
|---|---|---|---|---|---|
| 10 | 85.93 | 85.79 | 85.86 | HV0.5 | 125.8 |

| Indent No. | D1(µm) | D2(µm) | Davg(µm) | Hardness Type | Hardness (HV) |
|---|---|---|---|---|---|
| 31 | 113.18 | 112.63 | 112.9 | HV0.5 | 72.7 |

Fig. 4 (a) Cross-sectional view of LPBF printed circular Mg–2Ag–2Sn and Cp–Mg samples on an aluminium substrate; hardness measurement on the (b) aluminum substrate and (c) interface of the substrate and the LPBF printed Mg–2Ag–2Sn alloy, (d) the LPBF printed Mg–2Ag–2Sn alloy, and (e) LPBF printed Cp–Mg.

dislocations to bow and loop around obstacles, and grain boundaries act as barriers to slip transmission. Different models were used to calculate these contributions to the yield strength.[33,53–60] The Fleischer model is applied to calculate the $\Delta\sigma_{ss}$:[53,57–59]

$$\Delta\sigma_{ss} = kc^{2/3} \tag{6}$$

with $c$ being the total atomic fraction of solutes (Ag + Sn) in the $\alpha$-Mg matrix. Solute atoms of Ag and Sn substitute into the Mg lattice, producing localized lattice distortions that interact with

Table 2 Comparison of mechanical properties and corrosion rate of the present study with alloys in the literature

| Sample | Hardness ($H_v$) | Young's modulus (GPa) | Yield strength (MPa) | $E_{corr}$ (V) | $i_{corr}$ ($\mu$A cm$^{-2}$) | Corrosion rate (mmpy) | Ref. |
|---|---|---|---|---|---|---|---|
| Cp–Mg | 83 | 22.6 | 271.3 | −1.58 | 98.83 | 2.25 | Present work |
| Mg–2Ag–2Sn | 133 | 36.2 | 434.8 | −1.38 | 42.21 | 0.96 | Present work |
| Wrought Mg | 60 | — | — | — | — | — | 47 |
| AZ91D | 85–100 | — | 254 | | | — | 30 |
| WE43 | 87–96 | — | — | | | | — |
| WE43 | 74.7–95.3 | — | 250 | | | 0.65–0.68 | 16 |
| Human bone | 33.3–43.8 | 3–20 | 104–121 | | | — | 65–67 |

dislocation stress fields and increase the stress required to move them. EDS line scans in Fig. 3(c) and (d) depict $c_{Ag} \approx 0.33$ at% and $c_{Sn} \approx 0.51$ at%, so, $c \approx 0.84$ at%. In Mg binary alloys, strong solutes such as Ag and Sn typically exhibit the Fleischer-model constant $k$ in the order of 100–300 MPa.[61–64] Both Ag and Sn markedly strengthen Mg, with Ag showing particularly pronounced effects. A reasonable estimate for $k$ in Mg–Ag–Sn solid solutions lies between 150 and 250 MPa. The exact value depends on the relative concentrations and mutual interactions of Ag and Sn in the Cp–Mg matrix, but this range is consistent with the strong hardening observed in Mg–Ag and Mg–Sn systems. Thereby, choosing $k$ = 200 MPa yields $\Delta\sigma_{ss} \approx 200 \times 0.0084^{2/3} \approx 8.13$ MPa.

For Orowan strengthening, the classic Ashby–Orowan relation is used for Mg–2Ag–2Sn.[60]

$$\Delta\sigma_{\mathrm{Or}} = \frac{0.13\mathrm{Gb}}{\lambda}\ln\left(\frac{d}{2b}\right) \quad \text{with } \lambda = \frac{d}{2\sqrt{\frac{f}{\pi}}} \tag{7}$$

Here, $G \approx 17$ GPa and $b \approx 0.32$ nm for Mg, while SEM-based areal analysis on the LPBF specimens showed $Mg_2Sn$ needles with mean diameter $d \approx 1.2$ μm and volume fraction $f \approx 0.045$.[55] Dislocations must bow between these hard intermetallics. $\lambda$ represents the average interparticle spacing. Substituting these values gives $\lambda \approx 1.2\ \mu\mathrm{m}/(2\sqrt{(0.045/\pi)}) \approx 0.5\ \mu\mathrm{m}$, leading to $\Delta\sigma_{\mathrm{Or}} \approx 120$ MPa, reflecting the additional stress needed to loop dislocations around the $Mg_2Sn/Ag_3Sn$ particles.

Finally, grain-refinement strengthening was estimated *via* the Hall–Petch relation.[56]

$$\Delta\sigma_{\mathrm{HP}} = k_{\mathrm{HP}}(d^{-1/2} - d_0{}^{-1/2}) \tag{8}$$

where $k_{\mathrm{HP}} \approx 0.26$ MPa m$^{1/2}$ for Mg, $d_0$ (cast Mg grain size) $\approx 20$ μm, and $d$ (LPBF grain size) $\approx 8$ μm (from SEM). Thus, $\Delta\sigma_{\mathrm{HP}} \approx 80$ MPa. Grain boundaries serve as barriers to dislocation motion: as grains refine, the distance a dislocation can travel decreases, raising the stress for slip.

Summing these contributions, $\sigma_{\mathrm{predicted}}$ is calculated to be 422.5 MPa, which is a close approximation (within 10%) of our experimentally measured yield strength of ∼415 MPa. This close agreement validates that solid-solution (∼14.5 MPa), Orowan (∼120 MPa), and grain-refinement (∼80 MPa) mechanisms collectively account for the observed strengthening in the LPBF Mg–2Ag–2Sn alloy.

The corrosion tests conducted on the Cp–Mg and Mg–2Ag–2Sn alloys demonstrated that the presence of Ag and Sn in the Mg alloys improves their corrosion resistance, confirmed by the corrosion parameters determined from the Tafel plot (Fig. 5a; red color). Ag and Sn are well known to enhance the corrosion resistance properties of Mg alloys by forming different phases with Mg.[13,14] Different intermetallic phases of Mg–Sn, Mg–Ag, and Ag–Sn, which appeared in Fig. 2, enhance corrosion resistance by acting as a stable protective barrier against the incoming corrosive ions through the solution. Finely dispersed $Mg_2Sn$ and $Ag_3Sn$ in the sample, as observed in Fig. 3b, support uniform surface passivation.[32] $Mg_2Sn$ enhances the corrosion resistance of Mg alloys by forming stable passive layers, as reported previously.[13] Increasing the Sn content in Mg–Sn alloys enhances corrosion resistance.[68] Mg–10Sn alloys exhibit significantly lower corrosion rates and reduced cathodic activation compared to pure Mg.[68] While $Mg_2Sn$ intermetallic may initially promote pitting corrosion through cathodic sites, a passivation layer eventually forms, further improving corrosion resistance as reported previously.[69] Uniform distribution of $Mg_2Sn$ phases also helps reduce corrosion rates.[70] It has been reported that Ag in Al–Mg alloys enhances intergranular corrosion resistance by preventing certain phase formations and increasing the corrosion potential.[71] Similarly, $Mg_2Sn$ and $Ag_3Sn$ act as intermetallic phases, but their lower quantities can reduce the galvanic corrosion. In Mg–2Ag–2Sn alloys, lower quantities of $Mg_2Sn$ and $Ag_3Sn$ phases homogeneously and uniformly distributed within the alloys improve corrosion resistance by facilitating the formation of a stable, protective passivation layer.[70] While higher concentrations of these phases can cause Galvanic corrosion by acting as cathodes, lower amounts promote a more uniform phase distribution, reducing localized corrosion. This results in enhanced overall corrosion resistance as the passivation layer effectively protects the alloy matrix from degradation. It has been reported previously that a high corrosion potential and low corrosion current lead to a higher corrosion resistance for the alloy.[24,72,73] High corrosion potential and lower corrosion current values (Table S1) of the additively manufactured Mg–Ag–Sn alloy confirmed the enhanced corrosion resistance compared to Cp–Mg, which is an important attribute for the use of this alloy in biomedical applications.

Fig. 5b and c depict the results of EIS studies performed on the sample in the form of Nyquist and Bode plots. The Nyquist plot (Fig. 5b) depicts the presence of three loops, one high-frequency capacitance loop, one medium-frequency capacitance loop, and one low-frequency inductance loop. The medium-frequency capacitance loop reflects the influence of the surface film on corrosion, while the high-frequency loop corresponds to the relaxation process of electrochemical impedance, associated with sample degradation.[70,74] Polarization resistance ($R_p$) is a well-known parameter used to assess the corrosion resistance of a sample in corrosive environments.

$$R_p = R_{ct} + R_L \tag{9}$$

where $R_{ct}$ is the charge transfer resistance and $R_L$ represents the inductance resistance due to localized corrosion.

The radius of the circular loop in a Nyquist plot is directly proportional to ($R_p$) the corrosion resistance for the alloy system.[16,69,70,73,75] It can be observed from Fig. 5b that the resistance of the medium frequency capacitance loop is larger for the Mg–2Ag–2Sn alloy than that of Cp–Mg, which indicates that the surface film for the ternary alloy was more protective compared to that of pure Mg. Low-frequency region plots contribute to the pitting corrosion in the corrosion process.[70] All alloys exhibit an inductive loop at low frequencies, indicating pitting behavior and the breakdown of the corrosion product layer.[69] It is evident that the inductive resistance loop has a smaller diameter for the Mg–2Ag–2Sn alloy when compared to that of Cp–Mg, indicating that the corrosion product films or layers forming on the surface of pure Mg alloy are weak and break easily when compared to those of the alloy. The adherent protective film for the Mg–2Ag–2Sn alloy is evident from the smaller inductive loop (in Fig. 5c), which is attributed to the presence of Ag and Sn. Additionally, the charge transfer resistance ($R_{ct}$) and the polarization resistance ($R_p$) of the Mg–2Ag–2Sn alloy were higher than those of the Cp–Mg alloy. Thus, the Mg–2Ag–2Sn alloy has superior corrosion resistance due to the presence of various phases.

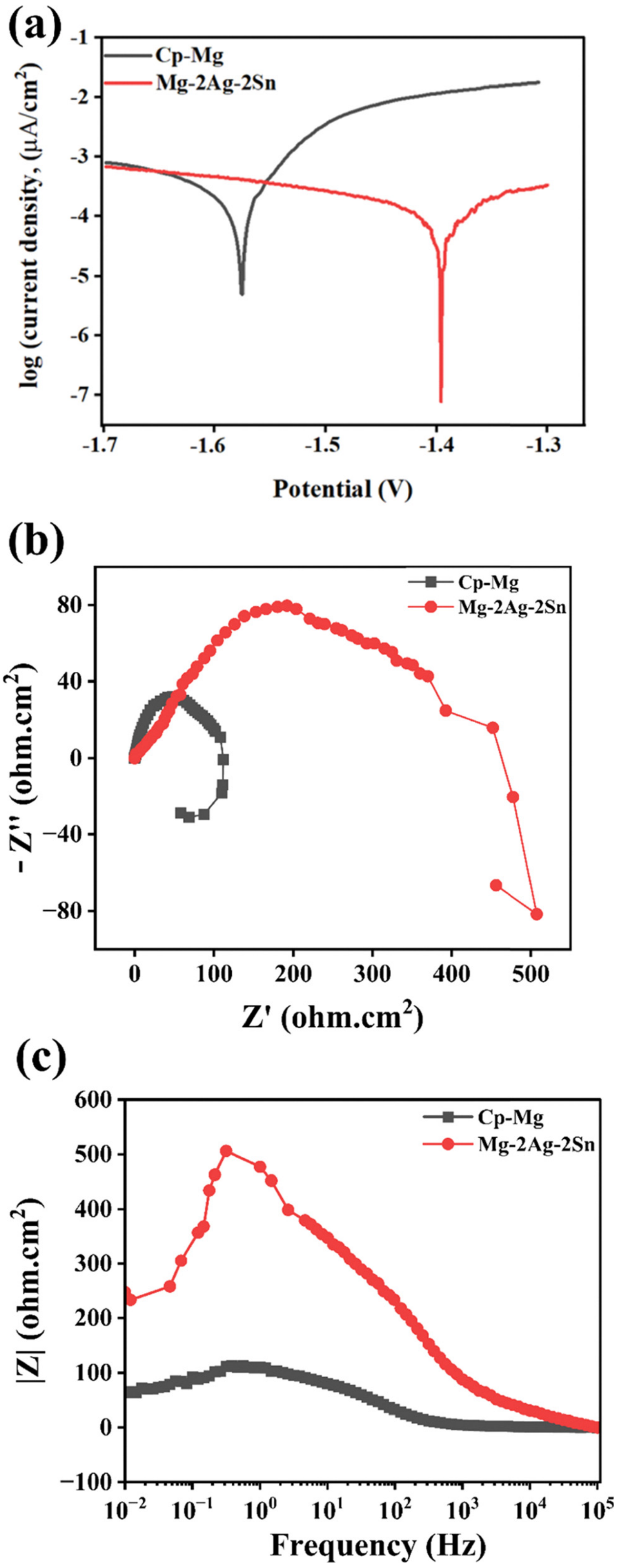

Fig. 5 (a) Tafel plot, (b) Nyquist plot, and (c) Bode plot of Cp–Mg and Mg–2Ag–2Sn circular samples prepared at optimized process parameters (T17).

The presence of higher impedance values in the Bode plot is considered an indication of higher corrosion resistance.[69] The Bode plot in Fig. 5c depicts the |$Z$|-frequency curve. Mg–2Ag–2Sn shows five-fold higher impedance values compared to the Cp–Mg alloy, which also indicates higher corrosion resistance. The increase in the overall corrosion resistance of the Mg–2Ag–2Sn alloy can be attributed to the formation of protective films of Sn reported previously.[76] The results of EIS studies agree with the Tafel findings. Previous studies have shown that the corrosion resistance of Mg alloys depends on the types, densities, distributions, and volume fractions of precipitates.[37–43] Additionally, defects such as pores or cracks accelerate the degradation of the matrix. Proper heat treatment enhances microstructural uniformity, eliminates defects, and promotes fine, evenly distributed precipitates, reducing micro-galvanic corrosion. As a result, uniform corrosion progresses more slowly, leading to a relatively stable corrosion film. In this study, the alloy shows low corrosion current density and high impedance values, which could be attributed to the formation of a protective surface film. Based on earlier reports, it is likely that finely dispersed intermetallic phases like $Mg_2Sn$ and $Ag_3Sn$ act as micro-cathodes that promote local alkalization during corrosion, leading to the formation of a two-layered passivation film. The inner layer is likely composed of $Mg(OH)_2$, which adheres well to the substrate, while the outer layer may consist of $SnO_2$ and possibly Ag-based compounds such as $Ag_2O$ or AgCl, which provide enhanced chemical stability. Prior work on Mg–Sn alloys shows that $SnO_2$ preferentially segregates at the outer film layer, imparting superior barrier properties *versus* pure $Mg(OH)_2$.[77] $Mg(OH)_2$ likely forms a more adherent inner layer, anchoring the passive film to the substrate.[16,24] The resulting bilayer, an inner Mg-based hydroxide overlain by a thin, dense $SnO_2$ network, resists $Cl^-$ penetration and minimizes localized dissolution. This synergy between $Mg_2Sn$ and $Ag_3Sn$ (which may similarly oxidize to $Ag_2O$/AgCl under chloride attack) plausibly enhances the overall impedance and suppresses pit initiation as observed in our electrochemical impedance spectra and polarization scans. The corrosion mechanism presumably involves micro-galvanic cells formed between the α-Mg matrix (anode) and the intermetallic particles (cathodes). Cathodic water reduction around these intermetallics likely raises the local pH, encouraging the precipitation of $Mg(OH)_2$ and tin oxides. Prior studies on Mg–Sn alloys show that $SnO_2$ enriches the outer layer and stabilizes it against $Cl^-$ attack.[78–81] Therefore, we surmise that, based on our high impedance and low $i_{corr}$ values, a similar mixed oxide is formed here in the current study. Although more work is warranted to establish the mechanism, this proposed mechanism is in good agreement with previous findings on Mg–Sn alloys, which report a bilayer oxide structure with $SnO_2$ enriching the outer surface. Such a configuration is believed to hinder chloride ion penetration and delay pit formation.

Additionally, the fine and uniform distribution of $Mg_2Sn$ and $Ag_3Sn$ in our alloy may help suppress deep pit formation, as observed in earlier laser-processed Mg alloys. Rather than initiating large pits, the intermetallics support rapid re-passivation and generate a more uniform corrosion morphology. Overall, while more detailed chemical analysis is needed, the current findings suggest that the alloy's corrosion resistance may arise from a synergistic oxide film structure, consistent with mechanisms reported in prior Mg–Sn systems. Previous reports show that in Mg–Sn alloys, Sn-rich phases typically dictate pit characteristics: in conventional cast Mg–Sn materials, coarse $Mg_2Sn$ particles often become pit initiation sites, producing deep, irregular cavities.[77,82,83] In contrast, LPBF specimens in the current study contain fine $Mg_2Sn$ needles ($\sim$1.2 μm long) and $Ag_3Sn$ nodules ($\sim$0.5 μm in diameter), uniformly dispersed at approximately 4.5 vol% and 1.2 vol%, respectively. This microstructure yields a high density of shallow, evenly distributed pits ($<$5 μm deep) rather than a few deep defects. Previous studies reported that such fine dispersions shift the pit morphology from hemispherical craters to stalactite-like, submicron surface features.[77] In our alloy, the mixed-oxide film forming around each microcell rapidly re-passivates local anodic sites, promoting a more uniform corrosion front and minimizing grain undercutting. A similar behavior has been observed in laser-processed Mg–Sn–Zn alloys, where submicron $SnO_2$ networks inhibit pit coalescence and lateral growth.[84]

Based on the measurements reported in this study, the corrosion rate was calculated for the current alloys using the following formula reported in the literature and listed in eqn (10).[73,85]

$$\text{Corrosion rate (mmpy)} = \frac{(3.16 \times 10^8 \times i_{\text{corr}} \times M)}{(z \times F \times \rho)} \tag{10}$$

where $i_{corr}$ is the corrosion current density in A cm$^{-2}$, $M$ is the molar mass of magnesium (24.15 g mol$^{-1}$), $F$ is the Faraday constant (96 500 C mol$^{-1}$), $z$ is the number of electrons transferred for each metal atom (2 electrons) and $\rho$ is the metal density (1.74 g cm$^{-3}$).

Previously reported data on Mg alloys processed by LPBF for biomedical applications are presented in Table 2 and compared with the outcomes of the present study. The corrosion rate of the current alloy system was calculated using two established methodologies from the literature, both yielding consistent results as shown in Table 2.[70,73] The hardness of the printed alloy was found to be comparable to that of the previously reported alloys. Additionally, Young's modulus ($E$) and yield strength ($Y_s$) closely align with those of human cortical bone. According to clinical recommendations, an ideal corrosion rate for orthopedic implants should be below 0.5 mmpy.[65] The degradation rate of the alloy in simulated body fluid (SBF) was found to be below this threshold, thereby fulfilling a key requirement for its suitability as a biodegradable biomedical implant.[65]

While indirect additive manufacturing approaches, such as solvent-cast extrusion, binder jetting followed by sintering, and paste extrusion, have successfully produced Cp–Mg components, direct fusion-based techniques, such as LPBF and wire-arc additive manufacturing (WAAM), have been limited to magnesium alloys.[86–89] Although preliminary or experimental efforts have attempted SLM with pure Mg powders, no reports have conclusively demonstrated the fabrication of fully dense, defect-free bulk parts *via* direct melting.[89] The processing of unalloyed Mg using such methods remains particularly challenging due to its high flammability, susceptibility to oxidation and evaporation, and a pronounced tendency toward porosity and cracking.[86,87] One combined computational and experimental study investigated melt-pool dynamics during SLM of pure Mg; however, it did not achieve or confirm successful printing of defect-free, consolidated bulk structures.[89] To the best of our knowledge, the processing of Cp–Mg *via* LPBF has not been reported. This work demonstrates the successful fabrication of pure Mg for the first time using LPBF, including the systematic optimization of process parameters. Despite substantial challenges in tuning the LPBF chamber environment, specifically powder deposition and material buildup, parameter refinement enabled the successful printing of continuous layers with thicknesses of approximately 600–700 μm. This deposition was sufficient to conduct a comprehensive evaluation of the material's properties, as presented herein. In addition, a novel Mg–2Ag–2Sn alloy, designed for biomedical applications, was fabricated using the optimized LPBF parameters, allowing for a comparative assessment with Cp–Mg.

## 4. Conclusion

In this study, additive manufacturing of Cp–Mg and Mg–2Ag–2Sn alloys by LPBF was successfully demonstrated. The alloy was realized by *in situ* alloying of pre-mixed elemental powders during LPBF, which overcomes a key limitation for the widespread adoption of these emerging technologies for processing different alloys. A laser power of 400 W and a scan speed of 0.03 m $s^{-1}$ were determined to be well-suited for processing the two alloys. The additively manufactured parts were found to contain α-Mg, $Mg_{0.42}Al_{0.58}$, $MgAl_2O_4$, and AlMg phases in both alloys, with additional peaks of $Mg_2Sn$, $AgMg_3$, $AgMg_4$, and $Ag_3Sn$ for the Mg–2Ag–2Sn alloy. The high corrosion potential, low corrosion current values, larger Nyquist loop diameters, and five times higher impedance values confirm the higher corrosion resistance of the Mg–2Ag–2Sn alloy compared to Cp–Mg. The incorporation of Ag and Sn into the alloy enhanced the hardness of Mg by 63%. Thus, the desired combination of mechanical properties and corrosion resistance of Mg–2Ag–2Sn compared to Cp–Mg demonstrates that LPBF is a viable route for the *in situ* production of the alloy. These findings have important implications in the fabrication of next-generation bioresorbable implants that are personalized to meet the individual needs of patients.

## Conflicts of interest

There is no conflict of interest.

## Data availability

Data will be made available by the authors on request.

The Supplementary Information file presents information on the chamber parameters, powder, and corrosion tests. See DOI: **https://doi.org/10.1039/d5ma00390c**

## Acknowledgements

AK acknowledges ICMR (Indian Council for Medical Research) for the postdoctoral fellowship (5/3/8/54/ITR-F/2022-ITR). Funding from IFCPAR/CEFIPRA (Project number 6508-3) is gratefully acknowledged.

## References

1 J. Bi, J. Shen, S. Hu, Y. Zhen, F. Yin and X. Bu, Microstructure and mechanical properties of AZ91 Mg alloy fabricated by cold metal transfer additive manufacturing, *Mater. Lett.*, 2020, **276**, 128185.

2 J. Liu, B. Yin, Z. Sun, P. Wen, Y. Zheng and Y. Tian, Hot cracking in ZK60 magnesium alloy produced by laser powder bed fusion process, *Mater. Lett.*, 301, **2021**, 130283.

3 J. Liang, Z. Lei, Y. Chen, W. Fu, X. Chen and S. Ma, Elimination of extraordinarily high cracking susceptibility of ZK60 Mg alloy fabricated by laser powder bed fusion, *Mater. Lett.*, 2022, **312**, 131731.

4 A. Kumar and P. Pandey, Statistical modelling of mechanical properties and bio-corrosion behaviour of Mg3Zn1Ca15Nb fabricated using microwave sintering, *J. Alloys Compd.*, 2020, **854**, 156211.

5 A. Kumar and P. M. Pandey, Investigations into Mechanical and Corrosion Properties of Mg-Based Biomaterial Sintered Using a Customized Die Setup Coupled with a Tube Furnace, *J. Mater. Eng. Perform.*, 2023, **32**, 8174–8184.

6 R. Chen, H. Wang, Z. Sun and B. He, Study of icosahedral quasi-crystalline phase T2-Al6CuLi3 and transformation in 2A97 Al-Li alloy fabricated by laser additive manufacturing, *Mater. Lett.*, 2022, **316**, 132014.

7 C. Wang, Y. Shuai, Y. Yang, D. Zeng, X. Liang, S. Peng and C. Shuai, Amorphous magnesium alloy with high corrosion resistance fabricated by laser powder bed fusion, *J. Alloys Compd.*, 2022, **897**, 163247.

8 G. Yang, W. Q. Zhang, J. Zhang, J. Z. Yi and Y. F. Cui, Evolution of microstructure of WE43 magnesium alloys fabricated by laser deposition manufacturing with subsequent friction stir processing, *Mater. Lett.*, 2023, **330**, 133218.

9 F. Bär, L. Berger, L. Jauer, G. Kurtuldu, R. Schäublin, J. H. Schleifenbaum and J. F. Löffler, Laser additive manufacturing of biodegradable magnesium alloy WE43: A detailed microstructure analysis, *Acta Biomater.*, 2019, **98**, 36–49.

10 M. Voshage, S. Megahed, P. G. Schückler, P. Wen, Y. Qin, L. Jauer, R. Poprawe and J. H. Schleifenbaum, Additive manufacturing of biodegradable Zn-xMg alloys: Effect of Mg content on manufacturability, microstructure and mechanical properties, *Mater. Today Commun.*, 2022, **32**, 103805.

11 A. Kumar and P. M. Pandey, Development of Mg based biomaterial with improved mechanical and degradation properties using powder metallurgy, *J. Magnesium Alloys*, 2020, **8**, 883–898.

12 A. Kumar and P. M. Pandey, Effect of ultrasonic assisted sintering on mechanical properties and degradation behaviour of Mg15Nb3Zn1Ca biomaterial, *J. Magnesium Alloys*, 2021, **9**, 1989–2008.

13 C. Zhao, F. Pan, S. Zhao, H. Pan, K. Song and A. Tang, Preparation and characterization of as-extruded Mg-Sn alloys for orthopedic applications, *Mater. Des.*, 2015, **70**, 60–67.

14 D. Tie, F. Feyerabend, N. Hort, D. Hoeche, K. U. Kainer, R. Willumeit and W. D. Mueller, *In vitro* mechanical and corrosion properties of biodegradable Mg-Ag alloys, *Mater. Corros.*, 2014, **65**, 569–576.

15 H. Hyer, L. Zhou, G. Benson, B. McWilliams, K. Cho and Y. Sohn, Additive manufacturing of dense WE43 Mg alloy by laser powder bed fusion, *Addit. Manuf.*, 2020, **33**, 101123.

16 C. Ling, Q. Li, Z. Zhang, Y. Yang, W. Zhou, W. Chen, Z. Dong, C. Pan and C. Shuai, Influence of heat treatment on microstructure, mechanical and corrosion behavior of WE43 alloy fabricated by laser-beam powder bed fusion, *Int. J. Extreme Manuf.*, 2023, **6**, 015001.

17 G. R. Chou, S. Huang and S. L. Sing, The effect of thermal rest time during in situ alloying of Ti41Nb through laser powder bed fusion, *Mater. Sci. Addit. Manuf.*, 2024, 3(3), 3506.

18 C. Shuai, Y. Zhao, Y. Deng and C. Gao, Heterogeneous grain structure in biodegradable Zn prepared via mechanical alloying and laser powder bed fusion for strength-plasticity synergy, *Virtual. Phys. Prototyp.*, 2024, **19**(1), e2317780.

19 N. Singh, K. P. Srikanth, V. Gopal, M. Rajput, G. Manivasagam, K. G. Prashanth, K. Chatterjee and S. Suwas, In situ production of low-modulus Ti-Nb alloys by selective laser melting and their functional assessment toward orthopedic applications, *J. Mater. Chem. B*, 2024, **12**, 5982–5993.

20 R. Kumar and R. K. Gautam, Investigation of sliding wear, electrochemical corrosion, and biocompatibility of Ti-Nb alloys for biomedical applications, *Mater. Today Commun.*, 2024, **41**, 110365.

21 R. Macias, P. Garnica González, L. Olmos, I. Alanis-Fuerte, O. Jimenez, F. Alvarado-Hernández, M. Velasco-Plascencia and J. A. Ávila-Olivera, In Situ Fabrication of Ti-xNb Alloys by Conventional Powder Metallurgy, *Coatings*, 2024, **14**(7), 897.

22 S. Gangireddy, B. Gwalani, K. Liu, E. J. Faierson and R. S. Mishra, Microstructure and mechanical behavior of an additive manufactured (AM) WE43-Mg alloy, *Addit. Manuf.*, 2019, **26**, 53–64.

23 M. Yadav, A. Kumar, D. Kumar, S. Nilawar, M. Amirthalingam, S. Suwas and K. Chatterjee, Wire arc additively manufactured nitinol with excellent superelasticity for biomedical applications, *J. Mater. Chem. B*, 2025, **13**, 8844–8865.

24 B. Das, M. Yadav, S. Kundu and T. Mandal, Evaluation of corrosion behaviour of turmeric-coated AZ51 alloy in simulated body fluid for biomedical applications, *Corros. Eng., Sci. Technol.*, 2023, **58**, 124–137.

25 A. Kumar and P. M. Pandey, Comparison of processing routes for efficacious fabrication of Mg3Zn1Ca15Nb biomaterial, *Mater. Manuf. Proc.*, 2021, 1–12.

26 EC-Lab®Software User's Manual.

27 S. Huang, R. L. Narayan, J. H. K. Tan, S. L. Sing and W. Y. Yeong, Resolving the porosity-unmelted inclusion dilemma during in situ alloying of Ti34Nb via laser powder bed fusion, *Acta Mater.*, 2021, **204**, 116522.

28 L. Jauer, W. Meiners, S. Vervoort, C. Gayer and N. A. Zumdick, Selective Laser Melting of Magnesium Alloys ProQuest document link Database copyright, 2025.

29 K. Wei, Z. Wang and X. Zeng, Influence of element vaporization on formability, composition, microstructure, and mechanical performance of the selective laser melted Mg-Zn-Zr components, *Mater. Lett.*, 2015, **156**, 187–190.

30 K. Wei, M. Gao, Z. Wang and X. Zeng, Effect of energy input on formability, microstructure and mechanical properties of selective laser melted AZ91D magnesium alloy, *Mater. Sci. Eng.: A*, 2014, **611**, 212–222.

31 R. Duan, S. Li, B. Cai, Z. Tao, W. Zhu, F. Ren and M. M. Attallah, In situ alloying based laser powder bed fusion processing of β Ti–Mo alloy to fabricate functionally graded composites, *Composites, Part B*, 2021, **222**, 109059.

32 C. Zhao, F. Pan, S. Zhao, H. Pan, K. Song and A. Tang, Preparation and characterization of as-extruded Mg-Sn alloys for orthopedic applications, *Mater. Des.*, 2015, **70**, 60–67.

33 D. Hu, Y. Wang, D. Zhang, L. Hao, J. Jiang, Z. Li and Y. Chen, Experimental Investigation on Selective Laser Melting of Bulk Net-Shape Pure Magnesium, *Mater. Manuf. Proc.*, 2015, **30**, 1298–1304.

34 S. A. Khairallah, A. T. Anderson, A. Rubenchik and W. E. King, Laser powder-bed fusion additive manufacturing: Physics of complex melt flow and formation mechanisms of pores, spatter, and denudation zones, *Acta Mater.*, 2016, **108**, 36–45.

35 X. He, J. W. Elmer and T. Debroy, Heat transfer and fluid flow in laser microwelding, *J. Appl. Phys.*, 2005, **97**(8), 084909.

36 V. M. Sample and L. A. Lalli, Effects of thermomechanical history on hardness of aluminium, *Mater. Sci. Technol.*, 1987, **3**, 28–35.

37 X. Huang and S. Huang, Macro-alloying Effects of Al and Ag on the Age-Hardening Behavior and Precipitates Microstructure of a Mg-4Sn Alloy, *Jom*, 2020, **72**, 1384–1394.

38 X. F. Huang and W. Z. Zhang, Improved age-hardening behavior of Mg-Sn-Mn alloy by addition of Ag and Zn, *Mater. Sci. Eng.: A*, 2012, **552**, 211–221.

39 S. H. Huang, Microstructure and Mechanical Properties of a Ag Micro-Alloyed Mg-5Sn Alloy, *J. Mater. Eng. Perform.*, 2018, **27**, 3199–3205.

40 W. Li, X. Huang and W. Huang, Effects of Ca, Ag addition on the microstructure and age-hardening behavior of a Mg-7Sn (wt%) alloy, *Mater. Sci. Eng.: A*, 2017, **692**, 75–80.

41 X. Huang, Y. Du, W. Li, Y. Chai and W. Huang, Effects of Ag content on the solid-solution and age-hardening behavior of a Mg-5Sn alloy, *J. Alloys Compd.*, 2017, **696**, 850–855.

42 S. Jayalakshmi, S. Sankaranarayanan, S. P. X. Koh and M. Gupta, Effect of Ag and Cu trace additions on the microstructural evolution and mechanical properties of Mg-5Sn alloy, *J. Alloys Compd.*, 2013, **565**, 56–65.

43 X. Huang, Y. Du, W. Li, Y. Chai and W. Huang, Effects of Ag content on the solid-solution and age-hardening behavior of a Mg-5Sn alloy, *J. Alloys Compd.*, 2017, **696**, 850–855.

44 S. Wei, T. Zhu, M. Hodgson and W. Gao, Effects of Sn addition on the microstructure and mechanical properties of as-cast, rolled and annealed Mg-4Zn alloys, *Mater. Sci. Eng.: A*, 2013, **585**, 139–148.

45 F. Qi, D. Zhang, X. Zhang and X. Xu, Effect of Sn addition on the microstructure and mechanical properties of Mg-6Zn-1Mn (wt%) alloy, *J. Alloys Compd.*, 2014, **585**, 656–666.

46 G. Lu, B. Sun, J. Wang, Y. Liu and C. Liu, High-temperature age-hardening behavior of Al–Mg–Si alloys with varying Sn contents, *J. Mater. Res. Technol.*, 2021, **14**, 2165–2173.

47 C. L. P. Silva, R. B. Soares, P. H. R. Pereira, R. B. Figueiredo, V. F. C. Lins and T. G. Langdon, The Effect of High-Pressure Torsion on Microstructure, Hardness and Corrosion Behavior for Pure Magnesium and Different Magnesium Alloys, *Adv. Eng. Mater.*, 2019, **21**(3), 1801081.

48 R. K. Mudanyi, C. L. Cramer, A. M. Elliott and D. Kumar, Effect of W and C addition on the microstructure and phase composition of W–ZrC composites prepared by using Zr2Cu alloy and variant reactant compositions, *Open Ceram.*, 2022, **12**, 100305.

49 B. Guillaume, F. Boschini, A. Rulmont, M. Ausloos and R. Cloots, Influence of the shaping effect on hardness

homogeneity by Vickers indentation analysis, *J. Eur. Ceram. Soc.*, 2006, **26**, 3191–3196.

50 P. Zhang, S. X. Li and Z. F. Zhang, General relationship between strength and hardness, *Mater. Sci. Eng.: A*, 2011, **529**, 62–73.

51 W. J. Sun, S. Kothari and C. C. Sun, The relationship among tensile strength, Young's modulus, and indentation hardness of pharmaceutical compacts, *Powder Technol.*, 2018, **331**, 1–6.

52 S. K. Ghosh and M. Yadav, Effects of Intercritical Annealing on Microstructure and Mechanical Properties of Low C-Mn Steels, *Metallogr., Microstruct., Anal.*, 2024, **13**, 817–831.

53 A. Akhtar, *Solid Solution Strengthening of Magnesium*, 1968.

54 S. K. Manjhi, P. Sekar, S. Bontha and A. S. S. Balan, *Additive manufacturing of magnesium alloys: Characterization and post-processing*, KeAi Publishing Communications Ltd., 2024, DOI: **10.1016/j.ijlmm.2023.06.004**.

55 T. R. Long and C. S. Smiths, Single-crystal elastic constants of magnesium and magnesium alloys.

56 H. Yu, Y. Xin, M. Wang and Q. Liu, Hall-Petch relationship in Mg alloys: A review, *J. Mater. Sci. Technol.*, 2018, **34**, 248–256.

57 R. L. Fleischert, Substitutional Solution Hardening.

58 A. Akhtars and E. T. Ghtsoonian, Solid Solution Strengthening Of Magnesium Single Crystals-I Alloying Behaviour In Basal Slip.

59 J. A. Yasi, L. G. Hector and D. R. Trinkle, First-principles data for solid-solution strengthening of magnesium: From geometry and chemistry to properties, *Acta Mater.*, 2010, **58**, 5704–5713.

60 M. F. Ashby, The deformation of plastically non-homogeneous materials, *Philos. Mag.*, 1970, **21**, 399–424.

61 B. Wiese, R. Willumeit-Römer, D. Letzig and J. Bohlen, Alloying effect of silver in magnesium on the development of microstructure and mechanical properties by indirect extrusion, *J. Magnesium Alloys*, 2021, **9**, 112–122.

62 W. L. Cheng, Q. W. Tian, H. Yu, H. Zhang and B. S. You, Strengthening mechanisms of indirect-extruded Mg-Sn based alloys at room temperature, *J. Magnesium Alloys*, 2014, **2**, 299–304.

63 B. Q. Shi, R. S. Chen and W. Ke, Solid solution strengthening in polycrystals of Mg-Sn binary alloys, *J. Alloys Compd.*, 2011, **509**, 3357–3362.

64 L. Tian, Y. Zhou, X. Jing, T. Zheng, S. Zhou, J. Zhang, P. Peng and A. Tang, Calculation of critical shear stress for binary magnesium alloys: A first-principles study, *Mech. Mater.*, 2023, **184**, 104711.

65 Y. Wen, Q. Liu, J. Wang, Q. Yang, W. Zhao, B. Qiao, Y. Li and D. Jiang, Improving in vitro and in vivo corrosion resistance and biocompatibility of Mg–1Zn–1Sn alloys by microalloying with Sr, *Bioact. Mater.*, 2021, **6**, 4654–4669.

66 X. He, Y. Li, D. Zou, H. Zu, W. Li and Y. Zheng, *An overview of magnesium-based implants in orthopaedics and a prospect of its application in spine fusion*, KeAi Communications Co., 2024, DOI: **10.1016/j.bioactmat.2024.04.026**.

67 W. Wei Wu, Y. Bin Zhu, W. Chen, S. Li, B. Yin, J. Zhao Wang, X. Juan Zhang, G. Bin Liu, Z. Sheng Hu and Y. Ze Zhang, Bone Hardness of Different Anatomical Regions of Human Radius and its Impact on the Pullout Strength of Screws, *Orthop. Surg.*, 2019, **11**, 270–276.

68 T. W. Cain, C. F. Glover and J. R. Scully, The corrosion of solid solution Mg-Sn binary alloys in NaCl solutions, *Electrochim. Acta*, 2019, **297**, 564–575.

69 P. Metalnikov, G. Ben-Hamu, D. Eliezer and K. S. Shin, Role of Sn in microstructure and corrosion behavior of new wrought Mg-5Al alloy, *J. Alloys Compd.*, 2019, **777**, 835–849.

70 L. Zhong, Y. Wang, H. Luo, X. Cui, Y. Zhang, B. Dou and J. Peng, Influence of aging prior to extrusion on the microstructure and corrosion resistance of Mg–8Sn–2Zn–0.2Mn alloy, *J. Alloys Compd.*, 2019, **780**, 783–791.

71 C. Guo, H. Zhang, Z. Wu, D. Wang, B. Li and J. Cui, Effects of Ag on the age hardening response and intergranular corrosion resistance of Al-Mg alloys, *Mater. Charact.*, 2019, **147**, 84–92.

72 M. Yadav, I. Dey and S. K. Ghosh, A comparative study on the microstructure, hardness and corrosion resistance of epoxy coated and plain rebars, *Mater. Res. Express*, 2022, **9**, 056504.

73 I. Dey, P. Manna, M. Yadav, N. Kumar Tewary, J. K. Saha and S. K. Ghosh, *S*tudy on the Perspective of Mechanical Properties and Corrosion Behaviour of Stainless Steel, Plain and TMT Rebars.

74 P. Peng Wu, F. Jun Xu, K. Kun Deng, F. Yin Han, Z. Zhong Zhang and R. Gao, Effect of extrusion on corrosion properties of Mg-2Ca-XAl (X = 0, 2, 3, 5) alloys, *Corros. Sci.*, 2017, **127**, 280–290.

75 Z. Hu, Z. Yin, Z. Yin, K. Wang, Q. Liu, P. Sun, H. Yan, H. Song, C. Luo, H. Guan and C. Luc, Corrosion behavior characterization of as extruded Mg-8Li-3Al alloy with minor alloying elements (Gd, Sn and Cu) by scanning Kelvin probe force microscopy, *Corros. Sci.*, 2020, **176**, 108923.

76 H. Wang, Y. Song, J. Yu, D. Shan and H. Han, Characterization of Filiform Corrosion of Mg–3Zn Mg Alloy, *J. Electrochem. Soc.*, 2017, **164**, C574–C580.

77 W. Jiang, J. Wang, W. Zhao, Q. Liu, D. Jiang and S. Guo, Effect of Sn addition on the mechanical properties and biocorrosion behavior of cytocompatible Mg–4Zn based alloys, *J. Magnesium Alloys*, 2019, **7**, 15–26.

78 J. Yang, C. D. Yim and B. S. You, Effects of Sn in $\alpha$-Mg matrix on properties of surface films of Mg-xSn (x = 0, 2, 5 wt%) alloys, *Mater. Corros.*, 2016, **67**, 531–541.

79 C. He, B. Luo, Y. Zheng, Y. Yin, Z. Bai and Z. Ren, Effect of Sn on microstructure and corrosion behaviors of Al-Mg-Si alloys, *Mater. Charact.*, 2019, **156**, 109836.

80 X. Liu, D. Shan, Y. Song, R. Chen and E. Han, Influences of the quantity of Mg2Sn phase on the corrosion behavior of Mg-7Sn magnesium alloy, *Electrochim. Acta*, 2011, **56**, 2582–2590.

81 J. Wang, Y. Li, S. Huang and X. Zhou, Study of the corrosion behavior and the corrosion films formed on the surfaces of Mg-xSn alloys in 3.5 wt% NaCl solution, *Appl. Surf. Sci.*, 2014, **317**, 1143–1150.

82 G. L. Song and A. Atrens, *Corrosion mechanisms of magnesium alloys*, Wiley-VCH Verlag, 1999, DOI: 10.1002/(SICI)1527-2648(199909)1:1<11::AID-ADEM11>3.0.CO;2-N.

83 M. Khorasanian, M. Yeganeh, N. Gholamzadeh and S. R. Alavi Zaree, Effect of Addition of Silver and Chilled Casting on Corrosion Behavior of AZ91 Magnesium Alloy, *Int. J. Metalcast.*, 2021, **15**, 1184–1196.

84 C. Shuai, Y. Zhou, X. Lin, Y. Yang, C. Gao, X. Shuai, H. Wu, X. Liu, P. Wu and P. Feng, Preparation and characterization of laser-melted Mg–Sn–Zn alloys for biomedical application, *J. Mater. Sci.: Mater. Med.*, 2017, **28**, 13, DOI: 10.1007/s10856-016-5825-z.

85 T. Bellezze, G. Giuliani and G. Roventi, Study of stainless steels corrosion in a strong acid mixture. Part 1: cyclic potentiodynamic polarization curves examined by means of an analytical method, *Corros. Sci.*, 2018, **130**, 113–125.

86 J. Chen and B. Chen, Progress in Additive Manufacturing of Magnesium Alloys: A Review, *Materials*, 2024, **17**, 3851.

87 S. Seetharaman, D. Sankaranarayanan and M. Gupta, *Magnesium-Based Temporary Implants: Potential, Current Status, Applications, and Challenges*, Multidisciplinary Digital Publishing Institute (MDPI), 2023, DOI: 10.3390/jfb14060324.

88 M. Salehi, D. W. K. Neo, V. Rudel, M. Stautner, P. Ganser, S. X. Zhang, H. L. Seet and M. L. S. Nai, Digital manufacturing of personalized magnesium implants through binder jet additive manufacturing and automated post machining, *J. Magnesium Alloys*, 2024, **12**(8), 3308–3324.

89 B. AlMangour, J. Cheng, D. Grzesiak, Y. J. Hwang and K. A. Lee, Fundamental Study on the Development of Pure Magnesium Parts by Additive Manufacturing: An Experimental and Computational Analysis, *Met. Mater. Int.*, 2023, **29**, 429–443.